APPLICATION OF AN ARTIFICIAL INTELLIGENCE SEGMENTATION FOR DEEP HYPERTHERMIA TREATMENT PLANNING IN THE PELVIC REGION

TOMAS DRIZDAL*, MAREK NOVAK

Czech Technical University in Prague, Faculty of Biomedical Engineering, Department of Biomedical Technology, nám. Sítná 3105, 272 01 Kladno, Czech Republic

* corresponding author: tomas.drizdal@fbmi.cvut.cz

ABSTRACT. During a microwave hyperthermia oncology treatment, the target region temperature is elevated to the temperatures of 40–44 °C, which improves the therapeutic effect of a standard radiotherapy and/or chemotherapy treatments. Amplitudes and phases of antenna input signals in the phased array setup surrounding the 3D patient model are optimised with respect to maximise the energy deposition in the target region. In this study, we successfully integrated an automatic artificial intelligence segmentation routine, used for patient-specific 3D model generation, into the hyperthermia treatment planning process. This allows us to apply more realistic patient 3D model for the online hyperthermia guidance including detailed retrospective analyses of the overall treatment quality, possibly leading to a widespread clinical use of the hyperthermia treatment planning.

KEYWORDS: Hyperthermia, specific absorption rate, phased array applicator, hyperthermia treatment planning.

1. INTRODUCTION

Microwave regional hyperthermia is an oncology treatment during which a target region is heated to the temperature range of 40–44 °C for the duration of 60–90 minutes [1]. It is typically applied in combination with radiotherapy or chemotherapy, utilising constructive interference from multiple external electromagnetic field (EM) sources, converted into a heat within the human body [2, 3]. Individual EM waves are produced by the antennas surrounding the body and forming the phased array regional hyperthermia microwave system [4, 5]. Amplitudes and phases of individual antenna input signals are optimised in order to obtain maximum energy deposition within the target region [6, 7]. This is achieved by applying the hyperthermia treatment planning (HTP) process in which a patient-specific 3D models created from computed tomography (CT) scan in combination with a model of the microwave phased array system for EM field simulations and optimisation is used [8, 9].

HTP is applied for online clinical guidance, the amplitudes and phases of individual antennas input signals to be adjusted during the treatment, if high temperature is measured outside the target region or if the patient complains [10, 11]. It is also used as an inclusion criterion for the hyperthermia treatment (HT) to test whether it is possible to heat selected target or if it is safe for the patient to undergo the treatment [12]. HTP also allows a detailed retrospective analysis of the entire treatment process and design of novel applicator systems [13, 14]. For all HTP applications, the patient 3D model is pivotal for a correct implementation of the selected HTP application. Currently, in clinical practice the 3D patient model usually consists of tissues discriminated by a CT scan, such as muscle, fat, bone, lung and internal air [15]. With the development of automatic segmentation routines based on atlas registration or artificial intelligence (AI) algorithms, generating complex 3D models for the HTP purposes becomes feasible [16–18].

The purpose of this study was to test the application of an automatic AI segmentation routine for deep HTP purposes in the pelvic region. From publicly available CT scans, we created a 3D patient-specific 3D model using the automatic artificial intelligence based segmentation available in TotalSegmentator extension of 3D Slicer [18–21]. This 3D model was then imported in Sim4Life (version 7.0, Zürich MedTech AG, Switzerland) for electromagnetic field simulations using a phased array system consisting of 12 dipole antennas operating at 100 MHz placed in two rings. We optimised amplitudes and phases of each antenna input signal in order to maximise the specific absorption rate (SAR) within the pancreas assigned as a HT target region. We compared clinically applied SAR quantities for the comparison of detailed patient-specific 3D model consisting of internal organs and for a 3D model in which all internal organs were assigned as muscle, representing the current standard clinical segmentation practice.

2. MATERIALS AND METHODS

2.1. SEGMENTATION OF THE CT IMAGES

First, we created a patient-specific 3D model from the series of the CT images available from the Cancer Imaging Archive [19, 20]. The selected CT dataset

was for a pancreatic cancer patient. This patient data group has a bad prognosis as the symptoms often appear in the later stage. The tumour is also present in challenging locations for the radiotherapy treatment [22]. The CT images were imported into the 3D Slicer (version 5.2.2) for the AI segmentation for internal organs using the Total Segmentator extension [18]. Two segmentations, using the "Body" and the "Total" options were created and saved in the *.nrrd format. We used the "Total" segmentation option, since it contains individual organs, however without fat tissue. For fat assignment, we used the "Body" segmentation, which ensures that each CT pixel is assigned to a specific tissue. Afterwards, we combined these two segmentations and merged corresponding tissues, such as all muscle and bone parts, into a single file in the *.vtk format inside MATLAB (version 9.13, Natick, Massachusetts, USA) using the list shown in Table 3 in the Appendices. Then, we imported the CT images to the iSeg (version 3.10.57.98, Zürich MedTech, Switzerland) along with the MATLAB file and assigned individual organs. For fat tissue delineation, we used the "Body" AI segmentation inside the 3D Slicer and for muscle tissue, we used a threshold operation inside iSeg. Since Virtual Population models used for various in-silico studies, including those in hyperthermia filed, contain cartilage, we manually segmented the cartilage as well [23]. Figure 1a) shows an example of the CT image and Figure 1b) the corresponding segmentation in iSeg. The whole process took 5 minutes of GPU computational time and 40 minutes of operational power from which the manual cartilage segmentation took 20 minutes.

2.2. Hyperthermia treatment planning setup

The selected HT applicator consisted of twelve 100 MHz dipole antennas placed in two rings within the 500 mm long elliptically-shaped shell with a width of 600 mm and a height of 500 mm. An elliptical shape was selected to obtain more uniform distance between the patient surface and the shell compared to a cylindrical setup. This 3D phased array system was positioned around the 3D model in order to place the target region (pancreas) into the centre of the applicator system and provide at least a 40 mm distance from the patient surface to the wire dipole antenna elements (Figure 2). We have selected pancreas as a target region in this study, which represents with respect to its shape and location, a challenging organ for the HT.

2.3. Electromagnetic field simulation

A harmonic signal with 15 periods at 100 MHz was used for the excitation of all 12 antenna elements in the phased array setup. A 5 mm global discretisation FDTD step with a refinement to 2 mm for the region within the shell and to 1 mm for the wire
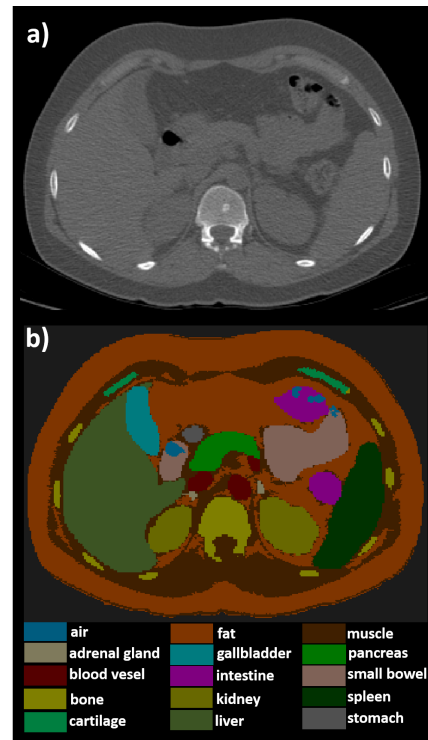

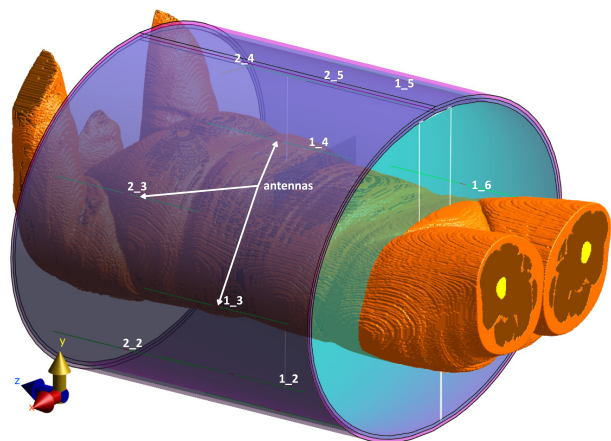Figure 1. a) axial CT image, b) segmented CT image in iSeg including internal organs.

Figure 2. HTP setup consisting of elliptical phased array (12 wire 100 MHz dipole antennas placed in two rings) and a patient-specific 3D model. Antenna names correspond to the ring and antenna number, e.g. antenna 2_4 is fourth antenna in second antenna ring.

dipole antenna was used. Absorbing UPML boundary conditions were placed 20 cm from the applicator model. The dielectric properties shown in Table 1 were assigned from the ITIS tissue database available in the Sim4Life package. All metalic parts were assigned as a perfect electric conductor (PEC) material. It took around 10 minutes to compute one EM field simulation accelerated by RTX 3080 Ti graphical processor unit.

Name	ϵ_r [−]	ρ [kg m^{-3}]	σ [S m^{-1}]
adrenal gland	64.2	1028	0.64
air	1	1.2	0
blood vessel	76.8	1050	1.23
bone	15.28	1908	0.06
cartilage	55.8	1100	0.47
esophagus	77.9	1040	0.9
fat	12.7	911	0.07
gallbladder	79	1071	1.01
heart	76.8	1050	1.23
kidney	98.1	1067	0.81
large intestine	81.8	1088	0.68
liver	69	1079	0.49
lung	31.6	394	0.31
muscle	66	1090	0.71
pancreas	68.8	1087	0.79
shell	2	1180	0.004
small intestine	96.5	1030	1.66
spleen	90.7	1089	0.8
stomach	77.9	1088	0.9
water	80	1000	0.002

TABLE 1. Dielectric properties at 100 MHz used in HTP [24, 25].

2.4. OPTIMIZATION AND EVALUATION

Individual EM field distributions were then imported to MATLAB for amplitude and phase optimisation of the antenna input signals using the particle swarm optimisation technique. We optimised the target to hot spot quotient (THQ) representing the ratio of averaged SAR inside the target region to the average SAR within the hotspot, which were assumed as a volume with 1 % highest SAR outside the target region [26]. Aside from the THQ (−), we evaluated the SAR target coverages (TC) parameters TC25 (%) and TC50 (%), determining the volume of tumour coverage with 25 % or 50 % SAR iso-contour. We have compared two models,

- *organs* – for this model, we assumed a complete segmentation including internal organs,

- *muscle* – for this model, we assigned all internal organs (except lung) as a muscle and cartilage was split into bone structure and muscle using histogram threshold segmentation, which is currently the clinically applied segmentation strategy for patient-specific 3D models used in HTP.

We also computed the absolute THQ difference |dTHQ| (%).

$$|\text{dTHQ}| = \left| \left(\frac{\text{THQ}_{\text{muscle}} - \text{THQ}_{\text{organs}}}{\text{THQ}_{\text{organs}}} \right) \right| \times 100 \quad (1)$$

where $|\text{THQ}_{\text{muscle}}|$ is the THQ value obtained using muscle patient model and $|\text{THQ}_{\text{organs}}|$ value obtained
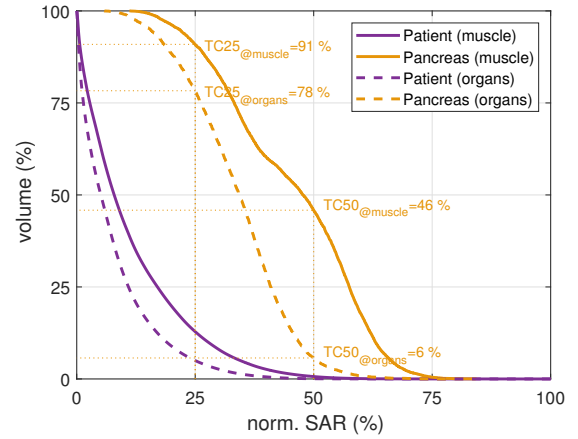

FIGURE 3. SAR volume cumulative histograms of pancreas and whole patient model for complete segmentation model (organs) and for model with organs assigned as muscle (muscle).

from complete segmentation model including internal organs.

3. RESULTS

The optimised power and phase coefficients of individual antenna input signals are shown in Table 2. Power coefficients are shown for 1 W of the total power of the phased array system.

Antenna	P_{organs} [W]	Φ_{organs} [°]	P_{muscle} [W]	Φ_{muscle} [°]
1_1	0.077	0	0.072	0
1_2	0.085	-5	0.103	24
1_3	0.087	140	0.069	78
1_4	0.029	-51	0.068	85
1_5	0.015	69	0.098	36
1_6	0.096	69	0.063	96
2_1	0.129	-8	0.075	6
2_2	0.122	49	0.108	93
2_3	0.083	3	0.079	54
2_4	0.100	-63	0.067	-3
2_5	0.098	-18	0.090	7
2_6	0.079	65	0.108	86

TABLE 2. Optimised powers P [W] (normalised to 1 W of the total power) and phases Φ [°] of antenna input signals for organs and muscle segmentations.

For the complete segmentation model including internal organs, we obtained TC25 = 78 %, TC50 = 6 % and THQ = 0.63, while for the model with internal organs assigned as muscle, TC25 = 91 %, TC50 = 46 % and THQ = 0.71, the |dTHQ| = 12.7 %. Figure 3 shows SAR cumulative histograms of the patient and pancreas for the detailed segmentation model including internal organs and for the patient-specific 3D model in which all internal organs were assigned as a muscle.
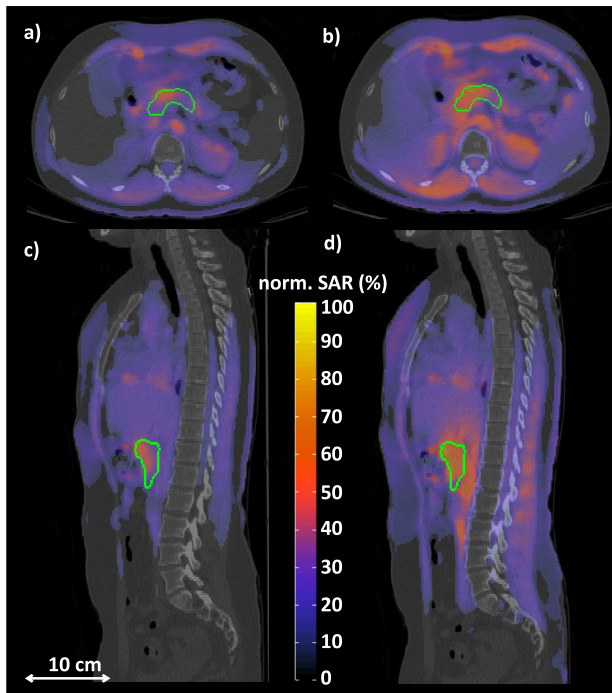
FIGURE 4. Normalized SAR CT overlay for complete segmentation model a) axial c) sagital slices and for model in which internal organs were assigned as muscle b) axial and d) sagital slices with highlighted pancreas contour in green.

Figure 4a) and Figure 4c) show axial and sagital slices of the optimised SAR for the complete patient model while Figure 4b) and Figure 4d) show the patient-specific 3D model with muscle dielectric properties assigned to organs.

4. DISCUSSION

We have successfully integrated AI automatic segmentation into our overall HTP process in the pelvic region. It takes around 45 minutes to generate detailed patient-specific 3D models used in automatically generated HTP setups. We received difference of 13 % for TC25 and 40 % for TC50 between the detailed segmentation including internal organs and the model segmented into muscle, fat, lung, air and bone, which is currently standard practice in clinical HTP. These differences, observed in the challenging pancreatic region, highlight the importance of implementing the detailed segmentation in this region. However, even with the detailed segmentation, we obtained TC25 = 78 %, which is considered to be sufficient (TC25 $\geq$ 75 %) for the HT. We estimated that manually creating a complete segmentation model would take an experienced individual around ten hours, which is significantly more than the 45 minutes required for the AI-assisted segmentation. We expect that this time will be further reduced in near future, to 25 minutes, by adding an automatic segmentation of the cartilage.

The observed difference in THQ of 12.7 % when comparing two studied models falls into a range of

7.0–22.8 % difference found by VilasBoas-Ribeiro et al. [15] when comparing a clinical model containing muscle, fat, bone, lung and internal air and a very detailed model of the Virtual Population models. These models are commonly used for in-silico studies of EM field exposure, nevertheless they represent healthy models of healthy volunteers which led to the development of Erasmus Virtual Patient Repository (EVPR) created from CT scans of real HT patients [27]. However, the EVPR models consist of a limited amount of tissues, such as fat, muscle, bone, internal air and tumour. The implemented AI segmentation allows to conduct simulation studies including temperature and thermoradiotherapy modelling with realistic patient 3D models [28–30]. These 3D models can be obtained from widely available public repositories, enabling non-clinical groups to also work in this area of research.

The optimised coefficients of antenna input signals differ between HTP results based on the muscle and organs segmentations. This was caused by different dielectric properties of individual organs with respect to muscle tissue. Tissue permittivity and conductivity influence the wavelength and attenuation of the propagating EM wave and thus also the optimised amplitudes and phases of individual antenna input signals. Predicting local areas with high temperatures (hot-spots), which usually appear at tissue interfaces with high dielectric contrast, might be improved with HTP based on a detailed segmentation. However, a study investigating whether a detailed segmentation leads to a higher EM dose within the target region and thus temperatures during the HT would need to be verified in clinical practice, which is outside the scope of this paper.

A total of 104 available tissues were segmented using the TotalSegmentator, which can also be used as constrained masks during the online optimisation of amplitudes and phases input signals of individual antennas in the phased array system. Detailed models also allow more accurate simulation guided design of HT devices using, for example, meta-material structures or compact antenna structures [31–33]. Furthermore, this technology might also enable the creation of more complex anthropomorphic phantoms for hyperthermia quality control measurements including dielectric properties of specific phantom materials [34–36]. In clinical practice, dielectric properties can be obtained individually for every patient using electric property tomography, which uses magnetic resonance imaging (MRI) scanner [37, 38]. MRI, along with Electric Impedance Tomography and Microwave Imaging, can be employed for non-invasive temperature monitoring during the HT, improving the overall treatment quality [39–42].

5. CONCLUSION

The implementation of an AI segmentation routine to create patient-specific 3D models enables a more re-

alistic and tailored HTP approach that can be applied in clinical practice. This could extend the availability of HTP treatment guidance to more clinics, improving the overall quality of HT. Detailed models are also suitable for testing the accuracy of temperature tissue model predictions.

REFERENCES

[1] N. R. Datta, D. Marder, S. Datta, et al. Quantification of thermal dose in moderate clinical hyperthermia with radiotherapy: a relook using temperature-time area under the curve (AUC). *International Journal of Hyperthermia* **38**(1):296–307, 2021.
https://doi.org/10.1080/02656736.2021.1875060

[2] H. Peeters, E. M. van Zwol, L. Brancato, et al. Systematic review of the registered clinical trials for oncological hyperthermia treatment. *International Journal of Hyperthermia* **39**(1):806–812, 2022.
https://doi.org/10.1080/02656736.2022.2076292

[3] J. L. Guevelou, M. E. Chirila, V. Achard, et al. Combined hyperthermia and radiotherapy for prostate cancer: a systematic review. *International Journal of Hyperthermia* **39**(1):547–556, 2022.
https://doi.org/10.1080/02656736.2022.2053212

[4] O. Fiser, I. Merunka, J. Vrba. Waveguide applicator system for head and neck hyperthermia treatment. *Journal of Electrical Engineering and Technology* **11**(6):1744–1753, 2016.
https://doi.org/10.5370/JEET.2016.11.6.1744

[5] H. P. Kok, E. N. K. Cressman, W. Ceelen, et al. Heating technology for malignant tumors: a review. *International Journal of Hyperthermia* **37**(1):711–741, 2020.
https://doi.org/10.1080/02656736.2020.1779357

[6] Z. Rijnen, J. F. Bakker, R. A. M. Canters, et al. Clinical integration of software tool VEDO for adaptive and quantitative application of phased array hyperthermia in the head and neck. *International Journal of Hyperthermia* **29**(3):181–193, 2013.
https://doi.org/10.3109/02656736.2013.783934

[7] D. Baskaran, K. Arunachalam. Implementation of thinned array synthesis in hyperthermia treatment planning of 434 MHz phased array breast applicator using genetic algorithm. *IEEE Journal of Electromagnetics, RF and Microwaves in Medicine and Biology* **7**(1):32–38, 2023. https://doi.org/10.1109/JERM.2022.3224294

[8] H. P. Kok, J. van der Zee, F. N. Guirado, et al. Treatment planning facilitates clinical decision making for hyperthermia treatments. *International Journal of Hyperthermia* **38**(1):532–551, 2021.
https://doi.org/10.1080/02656736.2021.1903583

[9] H. P. Kok, J. Crezee. Hyperthermia treatment planning: Clinical application and ongoing developments. *IEEE Journal of Electromagnetics, RF and Microwaves in Medicine and Biology* **5**(3):214–222, 2021. https://doi.org/10.1109/JERM.2020.3032838

[10] M. Franckena, R. Canters, F. Termorshuizen, et al. Clinical implementation of hyperthermia treatment planning guided steering: A cross over trial to assess its current contribution to treatment quality. *International Journal of Hyperthermia* **26**(2):145–157, 2010.
https://doi.org/10.3109/02656730903453538

[11] H. P. Kok, J. Crezee. Adapt2Heat: treatment planning-assisted locoregional hyperthermia by on-line visualization, optimization and re-optimization of SAR and temperature distributions. *International Journal of Hyperthermia* **39**(1):265–277, 2022.
https://doi.org/10.1080/02656736.2022.2032845

[12] M. M. Paulides, G. M. Verduijn, N. Van Holthe. Status quo and directions in deep head and neck hyperthermia. *Radiation Oncology* **11**(1):21, 2016.
https://doi.org/10.1186/s13014-016-0588-8

[13] R. Gaffoglio, M. Righero, G. Giordanengo, et al. Fast optimization of temperature focusing in hyperthermia treatment of sub-superficial tumors. *IEEE Journal of Electromagnetics, RF and Microwaves in Medicine and Biology* **5**(3):286–293, 2021.
https://doi.org/10.1109/JERM.2020.3043383

[14] T. Drizdal, K. Sumser, G. G. Bellizzi, et al. Simulation guided design of the MRcollar: a MR compatible applicator for deep heating in the head and neck region. *International Journal of Hyperthermia* **38**(1):382–392, 2021.
https://doi.org/10.1080/02656736.2021.1892836

[15] I. VilasBoas-Ribeiro, G. C. van Rhoon, T. Drizdal, et al. Impact of number of segmented tissues on SAR prediction accuracy in deep pelvic hyperthermia treatment planning. *Cancers* **12**(9):2646, 2020.
https://doi.org/10.3390/cancers12092646

[16] R. F. Verhaart, V. Fortunati, G. M. Verduijn, et al. CT-based patient modeling for head and neck hyperthermia treatment planning: manual versus automatic normal-tissue-segmentation. *Radiotherapy and Oncology* **111**(1):158–163, 2014.
https://doi.org/10.1016/j.radonc.2014.01.027

[17] V. Fortunati, R. F. Verhaart, W. J. Niessen, et al. Automatic tissue segmentation of head and neck MR images for hyperthermia treatment planning. *Physics in medicine and biology* **60**(16):6547, 2015.
https://doi.org/10.1088/0031-9155/60/16/6547

[18] J. Wasserthal, H.-C. Breit, M. T. Meyer, et al. TotalSegmentator: Robust segmentation of 104 anatomic structures in CT images. *Radiology: Artificial Intelligence* **5**(5):e230024, 2023.
https://doi.org/10.1148/ryai.230024

[19] K. Clark, B. Vendt, K. Smith, et al. The cancer imaging archive (TCIA): Maintaining and operating a public information repository. *Journal of Digital Imaging* **26**(6):1045–1057, 2013.
https://doi.org/10.1007/s10278-013-9622-7

[20] N. Mayr, W. T. Yuh, S. Bowen, et al. Cervical cancer – tumor heterogeneity: Serial functional and molecular imaging across the radiation therapy course in advanced cervical cancer (CC-tumor-heterogeneity), 2023. [2023-02-14]. https://doi.org/10.7937/ERZ5-QZ59

[21] A. Fedorov, R. Beichel, J. Kalpathy-Cramer, et al. 3D Slicer as an image computing platform for the Quantitative Imaging Network. *Magnetic Resonance Imaging* **30**(9):1323–1341, 2012. Quantitative Imaging in Cancer. https://doi.org/https://doi.org/10.1016/j.mri.2012.05.001

[22] A. van der Horst, H. P. Kok, J. Crezee. Effect of gastrointestinal gas on the temperature distribution in pancreatic cancer hyperthermia treatment planning. *International Journal of Hyperthermia* **38**(1):229–240, 2021. https://doi.org/10.1080/02656736.2021.1882709

[23] A. Christ, W. Kainz, E. G. Hahn, et al. The virtual family-development of surface-based anatomical models of two adults and two children for dosimetric simulations. *Physics in Medicine and Biology* **55**(2):N23, 2010. https://doi.org/10.1088/0031-9155/55/2/N01

[24] S. Gabriel, R. W. Lau, C. Gabriel. The dielectric properties of biological tissues: III. Parametric models for the dielectric spectrum of tissues. *Physics in Medicine and Biology* **41**(11):2271–2293, 1996. https://doi.org/10.1088/0031-9155/41/11/003

[25] P. Hasgall, F. D. Gennaro, C. Baumgartner, et al. ITIS database for thermal and electromagnetic parameters of biological tissues, 2018. [2022-02-23]. https://doi.org/10.13099/VIP21000-04-0

[26] R. A. M. Canters, P. Wust, J. F. Bakker, G. C. V. Rhoon. A literature survey on indicators for characterisation and optimisation of SAR distributions in deep hyperthermia, a plea for standardisation. *International Journal of Hyperthermia* **25**(7):593–608, 2009. https://doi.org/10.3109/02656730903110539

[27] G. G. Bellizzi, K. Sumser, I. VilasBoas-Ribeiro, et al. Standardization of patient modeling in hyperthermia simulation studies: introducing the Erasmus Virtual Patient Repository. *International Journal of Hyperthermia* **37**(1):608–616, 2020. https://doi.org/10.1080/02656736.2020.1772996

[28] I. VilasBoas-Ribeiro, S. A. N. Nouwens, S. Curto, et al. POD-Kalman filtering for improving noninvasive 3D temperature monitoring in MR-guided hyperthermia. *Medical Physics* **49**(8):4955–4970, 2022. https://doi.org/10.1002/mp.15811

[29] H. P. Kok, G. C. van Rhoon, T. D. Herrera, et al. Biological modeling in thermoradiotherapy: present status and ongoing developments toward routine clinical use. *International Journal of Hyperthermia* **39**(1):1126–1140, 2022. https://doi.org/10.1080/02656736.2022.2113826

[30] H. P. Kok, J. Crezee. Validation and practical use of Plan2Heat hyperthermia treatment planning for capacitive heating. *International Journal of Hyperthermia* **39**(1):952–966, 2022. https://doi.org/10.1080/02656736.2022.2093996

[31] D. Vrba, J. Vrba. Novel applicators for local microwave hyperthermia based on zeroth-order mode resonator metamaterial. *International Journal of Antennas and Propagation* **2014**:631398, 2014. https://doi.org/10.1155/2014/631398

[32] D. Vrba, J. Vrba, D. B. Rodrigues, P. Stauffer. Numerical investigation of novel microwave applicators based on zero-order mode resonance for hyperthermia treatment of cancer. *Journal of the Franklin Institute* **354**(18):8734–8746, 2017. https://doi.org/10.1016/j.jfranklin.2016.10.044

[33] D. Baskaran, K. Arunachalam. Design and experimental verification of 434 MHz phased array applicator for hyperthermia treatment of locally advanced breast cancer. *IEEE Transactions on Antennas and Propagation* **69**(3):1706–1715, 2021. https://doi.org/10.1109/TAP.2020.3016462

[34] T. Drizdal, M. M. Paulides, K. Sumser, et al. Application of photogrammetry reconstruction for hyperthermia quality control measurements. *Physica Medica* **101**:87–94, 2022. https://doi.org/10.1016/j.ejmp.2022.08.008

[35] T. Pokorny, D. Vrba, J. Tesarik, et al. Anatomically and dielectrically realistic 2.5D 5-layer reconfigurable head phantom for testing microwave stroke detection and classification. *International Journal of Antennas and Propagation* **2019**:5459391, 2019. https://doi.org/10.1155/2019/5459391

[36] O. Fiser, S. Ley, M. Helbig, et al. Temperature dependent dielectric spectroscopy of muscle tissue phantom. *International Journal of Microwave and Wireless Technologies* **12**(9):885–891, 2020. https://doi.org/10.1017/S1759078720000203

[37] E. Balidemaj, H. P. Kok, G. Schooneveldt, et al. Hyperthermia treatment planning for cervical cancer patients based on electrical conductivity tissue properties acquired in vivo with EPT at 3 T MRI. *International Journal of Hyperthermia* **32**(5):558–568, 2016. https://doi.org/10.3109/02656736.2015.1129440

[38] S. Gavazzi, C. A. T. van den Berg, A. Sbrizzi, et al. Accuracy and precision of electrical permittivity mapping at 3T: the impact of three , mapping techniques. *Magnetic Resonance in Medicine* **81**(6):3628–3642, 2019. https://doi.org/10.1002/mrm.27675

[39] I. VilasBoas-Ribeiro, S. Curto, G. C. van Rhoon, et al. MR thermometry accuracy and prospective imaging-based patient selection in MR-guided hyperthermia treatment for locally advanced cervical cancer. *Cancers* **13**(14):3503, 2021. https://doi.org/10.3390/cancers13143503

[40] T. V. Feddersen, D. H. J. Poot, M. M. Paulides, et al. Multi-echo gradient echo pulse sequences: which is best for PRFS MR thermometry guided hyperthermia? *International Journal of Hyperthermia* **40**(1):2184399, 2023. https://doi.org/10.1080/02656736.2023.2184399

[41] R. Poni, E. Neufeld, M. Capstick, et al. Feasibility of temperature control by electrical impedance tomography in hyperthermia. *Cancers* **13**(13):3297, 2021. https://doi.org/10.3390/cancers13133297

[42] O. Fiser, M. Helbig, J. Sachs, et al. Microwave non-invasive temperature monitoring using UWB radar for cancer treatment by hyperthermia. *PIER* **162**:1–14, 2018. https://doi.org/10.2528/pier17111609

A. APPENDICES

Tissue name in HTP	Tissue name from TotalSegmentator
adrenal gland	right_adrenal_gland, left_adrenal_gland
air	trachea
blood vessel	aorta, inferior_vena_cava, portal_vein, left_common_iliac_artery, right_common_iliac_artery, left_common_iliac_vein, right_common_iliac_vein
bone	L5_vertebra, L4_vertebra, L3_vertebra, L2_vertebra, L1_vertebra, T12_vertebra, T11_vertebra, T10_vertebra, T9_vertebra, T8_vertebra, T7_vertebra, T6_vertebra, T5_vertebra, T4_vertebra, T3_vertebra, T2_vertebra, T1_vertebra, C7_vertebra, C6_vertebra, C5_vertebra, C4_vertebra, C3_vertebra, C2_vertebra, C1_vertebra, left_rib_1, left_rib_2, left_rib_3, left_rib_4, left_rib_5, left_rib_6, left_rib_7, left_rib_8, left_rib_9, left_rib_10, left_rib_11, left_rib_12, right_rib_1, right_rib_2, right_rib_3, right_rib_4, right_rib_5, right_rib_6, right_rib_7, right_rib_8, right_rib_9, right_rib_10, right_rib_11, right_rib_12, left_humerus, right_humerus, left_scapula, right_scapula, left_clavicle, right_clavicle, left_femur, right_femur, left_hip, right_hip, Sacrum
esophagus	esophagus
fat	body
gallbladder	gallbladder, urinary_bladder
heart	heart, left_atrium, left_ventricle_of_heart, right_atrium, right_ventricle_of_heart, pulmonary_artery
kidney	right_kidney, left_kidney
large intestine	colon
liver	liver
lung	superior_lobe_of_left_lung, inferior_lobe_of_left_lung, superior_lobe_of_right_lung, middle_lobe_of_right_lung, inferior_lobe_of_right_lung
muscle	left_gluteus_maximus, right_gluteus_maximus, left_gluteus_medius, right_gluteus_medius, left_gluteus_medius, right_gluteus_medius, left_erector_spinae_muscle, right_erector_spinae_muscle, left_iliopsoas_muscle, right_iliopsoas_muscle
pancreas	pancreas
small intestine	small_bowel, duodenum
spleen	spleen
stomach	stomach

TABLE 3. Merging tissues from TotalSegmentator and its corresponding tissue names in HTP models.